Renewable Energy 278 (2026) 126655

Contents lists available at ScienceDirect

Renewable Energy

journal homepage: www.elsevier.com/locate/renene

Mechanistic insights into N_2O abatement over SFCMO-based direct ammonia solid oxide fuel cell: polarization behavior and environmental application

Celina Fernandes [a,b], Laura I.V. Holz [c,d], Francisco J.A. Loureiro [c,d], Sergey M. Mikhalev [c,d], Duncan P. Fagg [c,d,*], Adélio Mendes [a,b,**]

[a] LEPABE – Laboratory for Process Engineering, Environment, Biotechnology and Energy, Faculty of Engineering, University of Porto, Rua Dr. Roberto Frias, Porto, 4200-465, Portugal
[b] ALiCE – Associate Laboratory in Chemical Engineering, Faculty of Engineering, University of Porto, Rua Dr.Roberto Frias, Porto, 4200-465, Portugal
[c] TEMA – Centre for Mechanical Technology and Automation, Department of Mechanical Engineering, University of Aveiro, Aveiro, 3810-193, Portugal
[d] LASI – Intelligent Systems Associate Laboratory, Guimarães, 4800-058, Portugal

ARTICLE INFO

Keywords:
SOFC
Cathode
$Sr_2Fe_{1.5-x}Co_xMo_{0.5}O_{6-\delta}$
Nitrous oxide abatement
Ammonia
Double perovskite

ABSTRACT

Solid-oxide fuel cells (SOFCs) are investigated for N_2O abatement, targeting the decomposition of this potent greenhouse gas while generating electricity as by-product. Although O_2 is typically the oxidant in SOFCs, N_2O can also serve this role, as N_2O decomposes into N_2 and O_2 under operating conditions. This work analyzes a double-perovskite $Sr_2Fe_{1.45}Co_{0.05}Mo_{0.5}O_{6-\delta}$ (SFCMO) as a cathode for N_2O reduction. Dilatometry indicated an average thermal expansion coefficient of $10.7 \times 10^{-6}\,°C^{-1}$, compatible with common SOFC electrolytes. The SFCMO|GDC|YSZ|Ni-YSZ cell was tested with O_2 or N_2O, while the anode was fueled with NH_3. Electrochemical characterization of the cell was performed via electrochemical impedance spectroscopy (EIS) and distribution function of relaxation times (DFRT) between 600 and 750 °C. Analysis indicated that surface exchange was the rate-limiting step of the oxygen reduction reaction. N_2O as a source of oxygen atoms, which effectively lowers the oxygen partial pressure (p_{O_2}) at the cathode, may increase the concentration of oxygen vacancies and enhance surface redox activity. Accordingly, the cell supplied with N_2O exhibited more than a 30 % increase in power density compared to operation with O_2, with an average N_2O conversion of ~41.7 %. These findings demonstrate SFCMO electrode as an efficient electrocatalyst for N_2O abatement for intermediate-temperature SOFCs fueled by ammonia.

1. Introduction

In the context of the ongoing energy transition and climate change, the scientific community is compelled to develop energy-converting technologies that support a sustainable future. Nitrous oxide (N_2O), the third most potent greenhouse gas, poses a particular challenge due to its contribution to ozone layer depletion and the formation of acid rain. N_2O emissions are primarily associated with the nitric and adipic acids production, food-processing, and fossil fuel combustion [1]. The most widely adopted technology for N_2O abatement is Catalytic Decomposition. Nevertheless, this process employs noble metals, which are critical raw materials and very expensive [1]. In addition, O_2 species can interfere with the catalytic activity of the active sites by blocking them, making it difficult to achieve high or complete N_2O conversion [1]. Moreover, conventional catalytic decomposition requires high operating temperatures and does not enable energy recovery, which motivates the exploration of alternative approaches. Solid oxide fuel cell (SOFC) technology, based on an electrochemical ceramic membrane reactor, has attracted considerable attention for N_2O abatement from various emission sources [2]. In these systems, N_2O can be simultaneously decomposed while electricity is generated as a useful by-product. In this configuration, N_2O reduction and the oxygen reduction reaction (ORR)

* Corresponding author. TEMA – Centre for Mechanical Technology and Automation, Department of Mechanical Engineering, University of Aveiro, 3810-193, Aveiro, Portugal.
** Corresponding author. LEPABE – Laboratory for Process Engineering, Environment, Biotechnology and Energy, Faculty of Engineering, University of Porto, Rua Dr. Roberto Frias, 4200-465, Porto, Portugal.
E-mail addresses: duncan@ua.pt (D.P. Fagg), mendes@fe.up.pt (A. Mendes).

https://doi.org/10.1016/j.renene.2026.126655
Received 4 November 2025; Received in revised form 8 October 2026; Accepted 25 October 2026
Available online 26 October 2026
0960-1481/© 2026 The Authors. Published by Elsevier Ltd. This is an open access article under the CC BY license (http://creativecommons.org/licenses/by/4.0/).

occur at the cathode, whereas the anode is supplied with ammonia (NH_3) as a hydrogen source. Ammonia is an appealing fuel due to its established distribution infrastructure [3] and its abundant availability in nitric acid (HNO_3) production facilities, which are among the largest industrial emitters of N_2O.

Lowering SOFC operating temperatures from conventional 800-1000 °C range to intermediate temperatures (600-750 °C) is widely recognized as a key strategy for reducing material costs and improving system long-term durability. However, lower operating temperature adversely affect ORR kinetics, resulting in increased cathodic polarization and, consequently diminishing the overall SOFC performance [2].

Although cathodic processes in SOFCs have traditionally been investigated under O_2 - rich atmospheres, the use of unconventional oxidants, such as N_2O, may fundamentally alter the cathodic reaction pathways. In contrast to O_2 reduction, N_2O reduction involves coupled decomposition and oxygen incorporation processes [4], wish can significantly influence surface exchange kinetics, oxygen-vacancy chemistry, and polarization behavior. Therefore, the nature of the oxidant itself can directly affect ORR mechanisms and electrode performance. Despite the growing interest in N_2O-fed SOFCs, the electrochemical implications of operating cathodes under N_2O-containing atmospheres remain poorly understood, and mechanistic studies elucidating N_2O's impact on ORR kinetics are still scarce.

In this context, the development of suitable cathode materials represents a critical challenge for mitigating the performance losses with intermediate-temperature operation. Accordingly, identifying electrode materials that promote rapid surface exchange and efficient oxygen-ion transport in N_2O-containig atmospheres is essential for realizing high-performance N_2O-assisted SOFCs.

Among candidate materials, mixed ionic-electronic conducting (MIEC) perovskites have emerged as leading cathode options [5]. Their mixed conductivity extends of the electrochemical reaction zone beyond the triple-phase boundaries (TPB) to the entire electrode surface exposed to the gas-solid interface [6]. In particular, the double perovskite $Sr_2Fe_{1.5}Mo_{0.5}O_{6-\delta}$ (SFMO) has demonstrated very attractive properties (exceptional electronic (~20 S cm^{-1}) and oxide-ion (~0.13 S cm^{-1} at 800 °C) conductivities) and high structural stability in both oxidizing and reducing atmospheres [7], [8]. In this matter, literature says that by partial substituting Fe cations by Co at the B-site significantly improved ionic/electronic conductivity and electrochemical performance [9]. The substitution of Fe^{2+}/Fe^{3+} with Co^{2+}/Co^{3+} increased surface exchange kinetics by nearly two orders of magnitude, thereby enhancing catalytic activity without compromising structural stability. However, the Co content must be carefully optimized, as excessive substitution markedly increases the thermal expansion coefficient due to spin-state transitions of Co^{3+} [8], compromising thermomechanical compatibility with common electrolyte materials and potentially affecting long-term cell durability.

While SFMO electrode and its derivatives have been extensively investigated for standard SOFC applications [10], [11], its performance in N_2O-containing environments has received limited attention. Early work of Li et al. [12] demonstrated the feasibility of using SOFCs for N_2O abatement in a typical tubular reactor with a lanthanum strontium manganite (LSM)-YSZ cathode and a Ni–YSZ anode cermet, achieving ~60 % total N_2O conversion and a power density of 0.31 W cm^{-2}, which improved when air was replaced by N_2O. More recently, N_2O-fed SOFC employing $La_{0.6}Sr_{0.4}Co_{0.2}Fe_{0.8}O_{3-\delta} - Gd_{0.1}Ce_{0.9}O_{2-\delta}$ (LSCF-GDC) cathode reported high-performance (power densities of *ca.* 200 mW cm^{-2} at 650 °C), showing that replacing O_2 with N_2O can significantly affect cell performance [13]. Our group extended these approaches, demonstrating the feasibility of SFMO electrodes for non-Faradaic electrochemical modification of catalytic activity (NEMCA) in the N_2O reduction reaction [14]. Though these studies primarily focused on demonstrating feasibility and performance metrics, they provided limited insight into the fundamental mechanisms governing cathode operation under N_2O-containing atmospheres. In particular, the influence of N_2O on ORR kinetics, surface exchange processes, and oxygen vacancy-related phenomena remains largely unexplored.

The present work advances these findings by investigating $Sr_2Fe_{1.5-x}Co_xMo_{0.5}O_{6-\delta}$ (SFCMO), with $x = 0.05$, as a scarcely unexplored cathode material for the electrochemical reduction of N_2O in ammonia-fueled SOFC, operated at intermediate-temperatures, enabling simultaneous pollutant abatement and energy generation. Attention is devoted to elucidating the relationship between oxidant composition and cathode reaction mechanisms. Combining electrochemical impedance spectroscopy (EIS) with distribution function of relaxation times (DFRT) analyses, the influence of O_2- and N_2O-rich atmospheres on ORR kinetics, surface exchange processes, and polarization behavior can be systematically investigated. In addition, the thermomechanical compatibility of the Co-doped material is assessed through thermal expansion measurements.

To the best of our knowledge, this is the first mechanistic investigation of N_2O electroreduction on a Co-doped SFMO (SFCMO) cathode in a direct ammonia solid oxide fuel cell. Whereas our recent study on Co-doped SFMO cathodes [15] focused on microstructural optimization, the present work directly compares the electrochemical behavior under O_2 and N_2O-containing atmospheres. The results provide evidence that N_2O influences the cathodic reaction kinetics by altering surface oxygen coverage and oxygen-vacancy availability, thereby facilitating surface redox processes, providing mechanistic insight not previously reported for this cathode composition.

Beyond this fundamental contribution, the study demonstrates a potentially relevant technological concept in which N_2O mitigation is coupled with electricity generation from NH_3, a carbon-free fuel at the point of use. Under the investigated conditions, N_2O therefore exhibits a dual function: it is both a greenhouse-gas pollutant targeted for conversion and an oxidant capable of sustaining favorable cathodic electrochemical behavior. Collectively, these findings advance the understanding of N_2O electroreduction in intermediate-temperature SOFCs and are directly relevant to the development of sustainable energy-conversion technologies.

2. Experimental

2.1. Catalyst preparation

$Sr_2Fe_{1.45}Co_{0.05}Mo_{0.5}O_{6-\delta}$ (SFCMO) powder was synthesized via a sol-gel route [14]. Stoichiometric quantities of strontium nitrate ($Sr(NO_3)_2$), iron nitrate ($Fe(NO_3)_3$), and cobalt nitrate ($Co(NO_3)_2$), from Sigma Aldrich, >99 %, together with ammonium molybdate ($(NH_4)_6Mo_7O_{24}$, Sigma Aldrich, >99 %) were dissolved in distilled water. Ethylene diamine tetraacetic acid (EDTA), previously dissolved in ammonia solution, was then used as a complexing agent. The mixture was maintained at 90 °C and adjusted to a pH 10, making black. The obtained powder was calcined at 800 °C for 2 h using a heating/cooling rate of 3 °C min^{-1}. After calcination, the powder was ground in an agate mortar, pelletized and subjected to a second thermal treatment at 1200 °C in an atmosphere of air for 10 h. The Co doping level, $x = 0.05$ was selected based on structural stability considerations. Goldschmidt tolerance factor calculations indicated preservation of the double-perovskite structure at this low Co content, while circumventing structural instability and the formation of secondary phases at higher Co contents [16].

The crystal structure of the synthesized material was investigated by X-ray diffraction (XRD) using a *Rigaku SmartLab* diffractometer (Cu Kα radiation – 1.5406 Å, 40 kV, 30 mA). The diffraction patterns were collected over the range of $20° < 2\theta < 80°$ at a scan speed of 3° min^{-1}. Structural parameters were determined by Rietveld Refinement, employing the pseudo-Voigt peak profile function for the profile fitting and the B-spline function to model the background.

The thermal stability of the synthesized powder was assessed by thermogravimetric analysis (TGA) using a NETZSCH TG 209 instrument.

Measurement was carried out under synthetic air at 1150 °C, at a heating rate of 5 °C·min^{-1}, and a dwell time of 1 h. The thermal expansion behavior of the material was investigated using a L75 Horizontal Linseis dilatometer. The thermal expansion coefficient (TEC) was determined form the dimensional changes recorded between 300 and 1000 °C.

2.2. Fabrication of the membrane electrode assembly (MEA)

The present study was carried out using a commercial anode-supported half-cell (acquired from Elcogen). The cell consisted of a Ni/YSZ anode structure comprising an active fuel layer (Ni/8YSZ $(ZrO_2)_{0.92}(Y_2O_3)_{0.08}$), a support layer (Ni/3YSZ $(ZrO_2)_{0.97}(Y_2O_3)_{0.03}$) and a NiO contact layer. The anode support was coupled to a an yttria stabilized zirconia electrolyte (YSZ) and a gadolinia-doped ceria ($Ce_{0.8}Gd_{0.2}O_{2-\delta}$ - CGO20) buffer layer.

The cathode layer consisted of a screen-printed layer of ink containing the produced SFCMO onto the CGO20 buffer layer; the ink formulation consisted of the prepared SFCMO powder dispersed in a solution of 95 wt% of terpineol with 5 wt% of ethyl cellulose, using a powder-to-solution volume ration of 20:80. Stearic acid (3 wt%) was incorporated as a dispersant agent, and the mixture was homogenized in an agate mortar for 15 min. Two cathode layers were deposited by screen-printing and thermally treated at 350 °C for 1 h to remove the organic binders and subsequently sintered at 1000 °C for 4 h in an atmosphere of air, at a heating/cooling rate of 1.5 °C min^{-1}. The resulting working electrode exhibited an active area of 1.07 cm^2. A schematic representation of the 2-probe cell configuration employed in this work is presented in Fig. 1.

The final cell, a membrane electrode assembly (MEA), was assembled in a custom-designed reactor. Sealing was achieved using a glass-based sealant (Glass Powder G018-354 from SCHOTT) in a Crofer 22 APU support structure. The sealing process consisted of an initial dwell at 350 °C for 30 min, followed by heating to 850 °C for 1 h, using a heating/cooling rate of 2 °C min^{-1}. Electrical contact to both electrodes was established using a gold current-collecting grid (from Fiaxell) positioned on the cathodic and anodic sides of the cell.

2.3. Electrochemical experiments

Electrochemical Impedance Spectroscopy (EIS) and current-potential (*I-V*) difference characteristics of the of the cell were measured using an *Autolab* PGSTAT302 N potentiostat. The measurements were performed under combined atmospheres of pure NH_3 at the anode (50 mL min^{-1}) and pure O_2/N_2O at the cathode (50 mL min^{-1}) – the gas purities used were N_2 > 99.9995 %, NH_3 >99.996 %, N_2O >99.5 % and $O_2 \geq$ 99.9995 %, and were mixed using digital mass flow controllers. The electrochemical measurements were conducted between 600 and 750 °C, in the direction of decreasing temperature. A single MEA was use for both O_2 and N_2O experiments, with N_2O experiments performed first, followed by the O_2 experiments. The EIS data were recorded in the frequency range between 0.01 Hz and 1 MHz, with a signal amplitude of 50 mV to ensure a *quasi*-linear response and adequate signal-to-noise ratio at high operating temperatures, superimposed over various D.C. polarization potentials (−0.2, −0.4, −0.6, −0.8, −1 V). Equilibrium conditions were established by maintaining the cell at each target temperature for 1 h prior impedance measurements followed by repeated measurements after an additional hour under equal conditions. The resulting impedance data were analyzed by non-linear least square fitting using equivalent circuit models implemented in ZView© software (Scribner Associates), allowing the identification of the resistances and capacitances associated contributions associated with different individual processes. The impedance data were further evaluated using the Distribution Function of Relaxation Times (DFRT) approach. The DRTools software [17] was used to transform the EIS data from the frequency domain to the time domain into a DFRT spectrum. The inversion software, the DRTtools, is based on the *Tikhonov* regularization, which enables determination of distribution time function G(τ) [18].

The oxygen partial pressure of the exiting gas stream from the cathode was continuously monitored during polarization experiments, at 750 °C, using an 8YSZ oxygen sensor (from Kyocera, with platinum electrodes). The sensor measured the potential difference (ΔE) between reference gas - (air, with known oxygen partial pressure - p'_{O_2}) - and the cathodic gas outlet (p''_{O_2}), from which oxygen partial pressure was obtained by applying Nernst equation - Eq. (1):

$$\Delta E = E^0 + \frac{R\,T}{4\,F}\ln\left[\frac{p'_{O_2}}{p''_{O_2}}\right] \quad (1)$$

were R, F and T are universal gas constant (8.134 m^3 Pa K^{-1} mol^{-1}), the Faraday constant (96 845 C mol^{-1}) and the sensor temperature (K), respectively.

Since the oxygen released from the cathode originates from the reduction of N_2O at the cathode, the p_{O_2} value can be directly related to the extent of N_2O conversion. Considering N_2O reduction follows:

$$N_2O(g) \rightarrow N_2(g) + \frac{1}{2}O_2(g) \quad (1a)$$

the conversion of N_2O (X) in the single-cell can therefore be calculated from oxygen partial pressure as the gas composition is constrained by mass balance - the fractional sum of the different gases should be

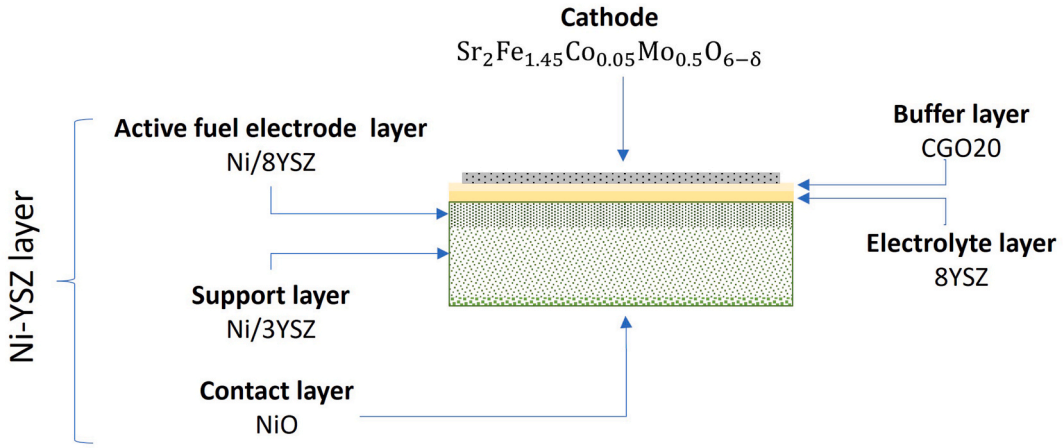


Fig. 1. – Schematic representation of the membrane electrode assembly.

unity:

$$p_{O_2} + p_{N_2} + p_{N_2O} = 1 \quad (2)$$

as well as (stochiometric conditions):

$$p_{N_2} = 2p_{O_2} \quad (3)$$

The N_2O conversion (X) (%) was, therefore, calculated as:

$$X\,(\%) = \left(1 - p_{N_2O}\right) \times 100 \quad (4)$$

Again, combining Eq. (1) and Eq. (2) can be rewritten as:

$$X\,(\%) = 3p_{O_2} \times 100 \quad (5)$$

3. Results and discussion

3.1. Structural characterization

Fig. 2 depicts the XRD pattern of the $Sr_2Fe_{1.45}Co_{0.05}Mo_{0.5}O_{6-\delta}$ (SFCMO) powder obtained after calcination at 1200 °C. The resultant pattern shows a pure SFCMO phase, exhibiting a cubic symmetry ($Fm\bar{3}m$ space group). The phase assignment was validated by comparison with PDF Card No: 01-079-7614 and is consistent with the developed work Xin Pan *et al.* [9]. In agreement with this investigation, the low Co substitution level ($x = 0.05$) does not induce significant structural distortion and preserves the cubic double-perovskite structure. Any peak shifts observed relative to SFMO were minor and are attributed to the partial replacement of Fe by Co at the B-site [19]. Table 1 shows the lattice parameters ($a = b = c = 7.8368$ (8) Å) obtained by Rietveld refinement, along with the respective quality statistical factors, χ^2 and S. Low χ^2 (where $\chi^2 = R_{wp}/R_{exp}$) value and S value near to 1 indicates the good quality of the fit.

Some authors observed that the structure of the double $Sr_2Fe_xMo_{2-x}O_{6-\delta}$ ($0.8 < x < 1.5$) is dependent on the iron content [20]. According Rao *et al.* [21], this family of materials remains stable across a broad compositional range of cation and associated oxygen contents. For most compositions, the system was reported to adopt a tetragonal double perovskite structure (space group *I4/mmm)*. Though, for $x > 1.2$, as in the case of present work $x = 1.45$, the system was shown to adopt a cubic structure in space group $Fm\ \bar{3}\ m$ [20], in agreement with the current results. The reason for the change in the structure has been attributed to the ordering of iron and molybdenum. Typically, the iron and molybdenum atoms exhibit a certain degree of ordering in the double perovskite structure ($A_2BB'O_6$) due to the size and charge difference between Fe^{3+}/Fe^{4+} and Mo^{6+}. Nevertheless, at high Fe/Mo ratio of 3:1, $Sr_2Fe_{1.5}Mo_{0.5}O_{6-\delta}$, this ordering progressively disappears, leading to a random distribution of and both atoms over the B and B′ sites [22], [23].

Table 1
– Rietveld refinement extracted parameters of SFCMO. R_{wp}, R_{exp}, χ^2 *and* S are statistical factors of Rietveld refinement quality.

Material	SFCMO
Space Group	$Fm\bar{3}m$ (Cubic symmetry)
Lattice parameter ($a = b = c$)/Å	7.8368 (8)
Phase angle ($\alpha = \beta = \psi$)/°	90
R_{wp}/%	3.76
R_{exp}/%	2.85
χ^2	1.3905
S	1.1792

Afterwards, a thermogravimetric analysis (TGA) was performed to measure the lattice oxygen loss promoted by the reduction of metal ions during heating in air.

Fig. 3 shows the overall weight change during heating of the SFCMO sample, revealing a weight loss of 2.2 %, associated with oxygen loss and consequent oxygen vacancy formation. Here, the electrons required to maintain charge balance can be accommodated by the partial reduction of the B-site cations, leading to the formation of Fe^{4+}/Fe^{3+}, Mo^{6+}/Mo^{5+}, and Co^{4+}/Co^{3+} pairs [5]. The following equations that describe this behavior can be written using the *Krögger-Vink* notation as follows:

$$O_O^x(s) + 2Fe_{Fe}^x(s) \leftrightarrow 2Fe_{Fe}'(s) + \frac{1}{2}O_2(g) + V_O^{\bullet\bullet}(s) \quad (6)$$

$$O_O^x(s) + 2Mo_{Mo}^x(s) \leftrightarrow 2Mo_{Mo}'(s) + \frac{1}{2}O_2(g) + V_O^{\bullet\bullet}(s) \quad (7)$$

$$O_O^x(s) + 2Co_{Co}^x(s) \leftrightarrow 2Co_{Co}'(s) + \frac{1}{2}O_2(g) + V_O^{\bullet\bullet}(s) \quad (8)$$

The thermal expansion of the produced material was also evaluated by dilatometry, and the results are presented in Fig. 4. The calculated coefficient of thermal expansion (CTE, α) is $10.7 \times 10^{-6}\,°C^{-1}$. Despite cobalt doping, which is reported to cause an increase in the CTE [8], this value was found to be compatible with YSZ electrolyte, $10.7 \times 10^{-6}\,°C^{-1}$ [24]; an improved match when compared to average CTE of Co-based perovskites ($20 \times 10^{-6}\,°C^{-1}$ [9]) or compared to LSM, one of the most studied perovskites for SOFC (14–15.2 $\times 10^{-6}\,K^{-1}$ [25]) and compatible with YSZ electrolyte, $10.5 \times 10^{-6}\,°C^{-1}$ [24].

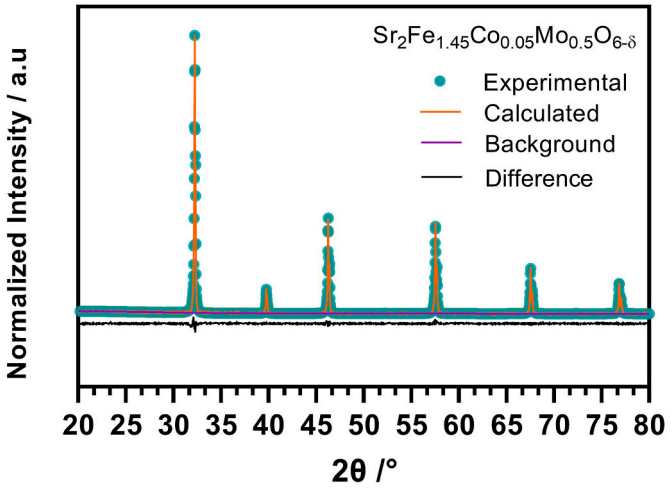


Fig. 2. – XRD pattern with Rietveld refinement analysis of the SFCMO powder obtained under air atmosphere after calcination at 1200 °C.

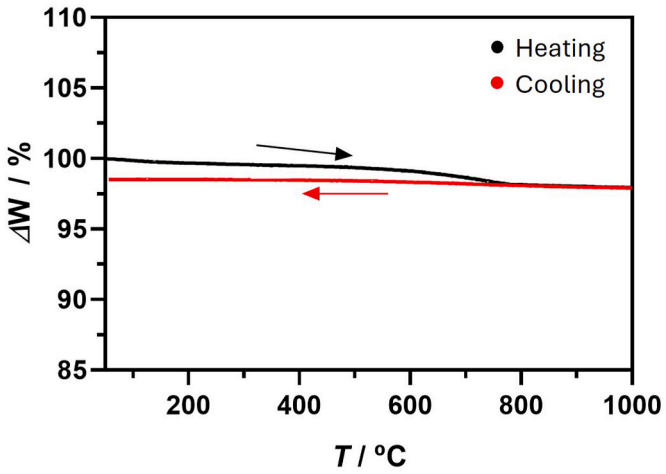


Fig. 3. – Thermogravimetry results of the SFCMO in air.

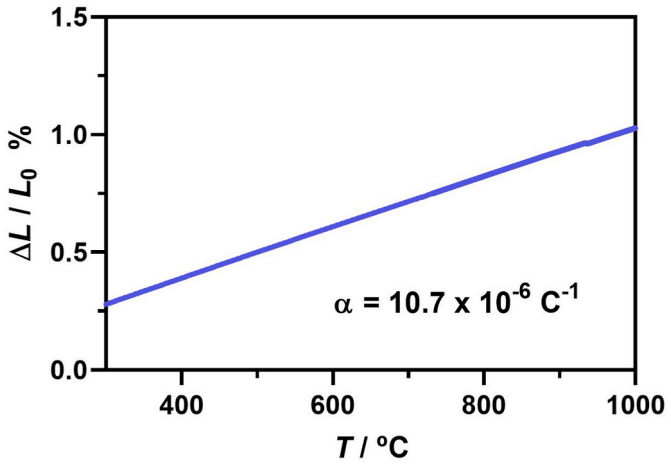


Fig. 4. – Dilatometry results of the SFCMO performed in air.

3.2. Electrochemical characterization

3.2.1. Open circuit potential (OCP) conditions

Fig. 5 depicts the Nyquist plots obtained in the experiments performed in the cell composed of SFCMO||CGO||YSZ||NiO at 750 °C under open circuit potential (OCP) conditions. Fig. 5 a) and b) depict the cell response under O_2 and N_2O atmospheres, using NH_3 as fuel, respectively.

The two Nyquist plots evidence the presence of at least two distinct limiting processes at high frequencies (HF) and intermediate frequencies (IF), along with a third process at low frequencies (LF) that only appears during cell operation in N_2O/NH_3. Therefore, the experimental data were fitted to two distinct equivalent circuit models (ECMs) to accommodate these responses. These models include an inductor (L_0), arising from the wiring and electrical connectors in the setup, in series with a resistor (R_0), which accounts for the ohmic contribution. This configuration is followed by two or three R||CPE components arranged in parallel, depending on whether two or three semi-circles were observed. Each R||CPE component consists of a resistor in parallel with a constant phase element, typically used to describe a semicircle in the frequency domain. The CPE substitutes for an ideal capacitor due to the necessity of accounting for non-ideal behavior in real electrochemical systems [26].

The fitting curves (solid red lines in Fig. 5) closely match the experimental data, indicating a good fit for the selected ECMs. Furthermore, the Kramers-Kronig (KK) validation (spectra in solid green lines in Fig. 5) exhibits a good agreement with the experimental Nyquist plots, supporting the consistency of the impedance measurements and confirming that the system responded within a linear regime The total polarization resistance (R_p) was calculated as the sum of the individual contributions: $R_p = R_1+R_2+(R_3)$, where R_1, R_2, and R_3 correspond to the polarization resistances occurring at high, intermediate, and low frequencies, respectively. The resulting data extracted from the equivalent circuit analysis are summarized in Table 2.

The ohmic resistance (R_0) is similar for the two cases, denoted to be effectively independent of any changes in the oxygen partial pressure (p_{O_2}) that could have resulted from switching from O_2 to N_2O atmospheres. The similarity in ohmic resistance observed in both cases is primarily attributed to the YSZ electrolyte layer in the MEA configuration. Since YSZ has a large electrolytic domain, it governs the ionic transport properties of the cell, leading to a nearly constant value of R_0 in both cases, regardless of the conditions [27]. Although the ohmic resistance is mainly associated with the YSZ electrolyte, a minor contribution from the CGO interlayer cannot be excluded. Since the CGO interlayer is located in the oxidant side of the cell, it should remain under oxidizing conditions during OCP measurements. Therefore, the partial reduction of Ce^{4+} to Ce^{3+}, which is known to introduce electronic conductivity in CGO under low oxygen partial pressures [28], is not expected to occur under the operating conditions reported in this work. Then, any contribution of the CGO interlayer to the measured ohmic resistance (R_0) in OCP is expected to arise predominantly from ionic conduction.

Table 2
– Fitting results for the Nyquist plots and the calculated polarization resistances from the selected equivalent circuit models (ECMs); *C*, *R*, and *W* are the capacitance, resistance, and the relaxation frequency of each process, respectively.

Gas composition	NH_3-O_2	NH_3-N_2O
R_0/Ω cm^2	5.82	4.92
R_1/Ω cm^2	11.3	7.35
C_1/F cm^{-2}	1.58×10^{-6}	2.12×10^{-6}
W_1/Hz	8.94×10^{3}	1.02×10^{4}
R_2/Ω cm^2	2.95	1.50
C_2/F cm^{-2}	4.55×10^{-3}	5.10×10^{-3}
W_2/Hz	1.19×10^{1}	2.08×10^{1}
R_3/Ω cm^2	-	2.08
C_3/F cm^{-2}	-	1.33×10^{-1}
W_3/Hz	-	0.575
R_p/Ω cm^2	14.25	10.93

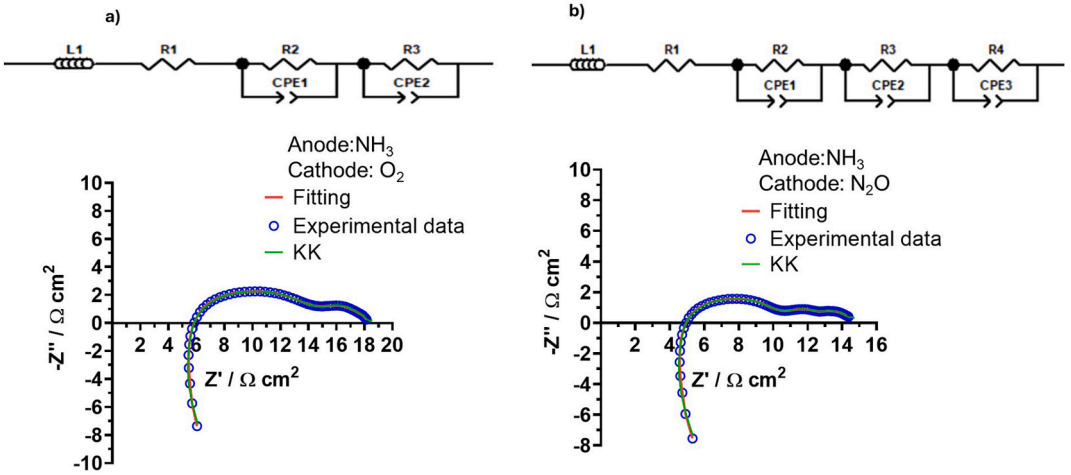


Fig. 5. Impedance spectra of the SFCMO||CGO||YSZ||NiO MEA measured at 750 °C under open circuit potential in a) NH_3 and O_2 and b) in NH_3 and N_2O.

The Nyquist plots obtained from experiments performed either under NH_3/O_2 and NH_3/N_2O present a high-frequency process (W_1 ~10^3 – 10^4 Hz) and an intermediate-frequency process (W_2 ~10^1 Hz). Noteworthy, a third arc in the low frequency region (W_3 ~10^{-1} Hz) is denoted in the cell using N_2O as oxidant. Therefore, to try to understand the origin of each of these contributions, we will now discuss the possible (electro)chemical reactions that are expected to occur simultaneously in both electrodes. In the cathode, the introduction of N_2O is anticipated to initially undergo decomposition into nitrogen and oxygen, as described by Eq. (1) - $N_2O(g) \rightarrow N_2(g) + \frac{1}{2}O_2(g)$, with subsequent oxygen reduction to O^{2-}, following the cathodic half-reaction,

$$O_2(g) + 2e^-(s) \rightarrow 2O^{2-}(s) \quad (9)$$

However, when directly feeding O_2 to the cathode, only Eq. (9) is expected to occur, leading to a different response of the cathodic electrode. Conversely, in the case of the anode, NH_3 reforming can follow two different pathways, the indirect route via ammonia cracking (Eq. (10)) followed by chemical oxidation of formed H_2 (Eq. (11)), the direct electrochemical oxidation of NH_3 (Eq. (12) or/and (13) or the combination of both [29], [30], [31].

$$NH_3(g) \leftrightarrow \frac{3}{2}H_2(g) + \frac{1}{2}N_2(g) \quad (10)$$

$$H_2(g) + O^{2-}(s) \rightarrow H_2O(g) + 2e^-(s) \quad (11)$$

$$2NH_3(g) + 3O^{2-}(s) \rightarrow N_2(g) + 3H_2O(g) + 6e^-(s) \quad (12)$$

$$2NH_3(g) + 5O^{2-}(s) \rightarrow 2NO(g) + 3H_2O(g) + 10\,e^-(s) \quad (13)$$

The high-frequency process is typically related to the double-layer capacitance (C_1 ~ 10^{-6} F cm^{-2}), as anticipated for the ion conduction and charge transfer to the triple phase boundaries (TPBs) for both oxygen reduction reaction (ORR) and hydrogen oxidation reaction (HOR) [32]. On the other hand, the intermediate-frequency process was assigned to the mass transport (C_2 ~10^{-3} F cm^{-2}), *e.g.*, bulk/surface oxygen diffusion in the cathode [33], [34] and surface hydrogen diffusion in the anode, toward the TPB [34]. Finally, the low-frequency process is indicative of gas phase diffusion/conversion limitations (C_3 ~ 10^{-1} F cm^{-2}) [32], [33], [34].

According to the literature, the Ni-YSZ anode has low catalytic activity for NH_3 reforming at intermediate temperatures (below 800 °C). As a result, complete conversion of NH_3 is not achieved under these conditions [32]. Therefore, the concentration of gaseous H_2 available for the anodic reaction is expected to be limited by the extent of ammonia decomposition when NH_3 is used as a fuel. Nevertheless, the additional low-frequency contribution is only observed when N_2O is used as an oxidant. As such, the origin of this contribution is unlikely to relate to the anode reaction, which remains constant in both experiments. Instead, it is more likely that the relatively lower oxygen availability in the case of N_2O atmosphere may lead to gas diffusion/concentration limitations between the bulk and gas phases and the reaction sites within the porous electrode [27], [34]. Under such conditions, the reduced rate of O_2 transport to the reaction sites limits the steady supply of oxygen ions across the electrolyte, thereby accounting for the additional concentration polarization observed when N_2O is used as oxidant. Fig. 6 depicts the temperature dependence of the polarization resistances (total polarization- R_p, high-frequency - R_1, intermediate-frequency - R_2, and low-frequency – R_3) obtained for the SFCMO||CGO20||YSZ||Ni-YSZ cell measured in the temperature interval of 600 – 750 °C under open circuit potential (OCP) conditions.

Fig. 6 a) and b) show the results for the cell when fed with NH_3/O_2 and NH_3/N_2O, respectively. No significant differences are observed for the activation energy (E_a) values of resistances R_p, R_1, and R_2, for both conditions. This suggests that the mechanisms governing these processes remain nearly the same in both O_2 and N_2O atmospheres. On the other hand, the magnitude of R_p, R_1, and R_2 is significantly lower when N_2O is used as an oxidant, for the entire temperature range. This suggests improved kinetics when N_2O oxidant is fed, and the underlying mechanisms will be further explored in the next section, where experiments conducted under polarization conditions are discussed.

Resistance R_3 was only observed when the cell was fed with NH_3/N_2O (lower oxygen concentration cathodic atmosphere) and shows almost no dependency on the operating temperature. These findings support the previous analysis that this response originates from diffusion/conversion-related processes, as diffusional transport and adsorption of species typically display limited dependency on the temperature [35], [36]. At 600 °C, the magnitude of R_3 was probably out of the frequency window of the measurement. To corroborate the choice of the equivalent circuit model, the Distribution Function of Relaxation Time (DFRT) was computed for the temperature range of 600 – 750 °C – Fig. 7. The DFRT spectra obtained when the cell was fed with NH_3/N_2O (Fig. 7a) confirm the presence of a small low-frequency peak (P_3) for all studied temperatures. In contrast, the DFRTs obtained when the cell was fed with NH_3/O_2 (Fig. 7b) do not show the presence of P_3, concurring with the above discussion of this process. The high-frequency process P_1 was observed at characteristic relaxation times of the order of 10^{-5}-10^{-4} s, whereas P_2 and P_3 appeared at longer relaxation times (10^{-3}-10^{-2} s and 10^{-1} s, respectively), consistent with charge-transfer and surface-related phenomena.

Finally, concerning the reaction kinetics, the ratio P_1/P_2+P_3, commonly used as an indicator of the predominant process [32], remains above unity. This indicates that ion conductivity and charge transfer at the triple-phase boundaries (TPBs) constitute the rate-limiting steps governing overall cell response, involving contributions from both cathodic oxygen reduction reaction (ORR) and the anodic hydrogen oxidation reaction (HOR).

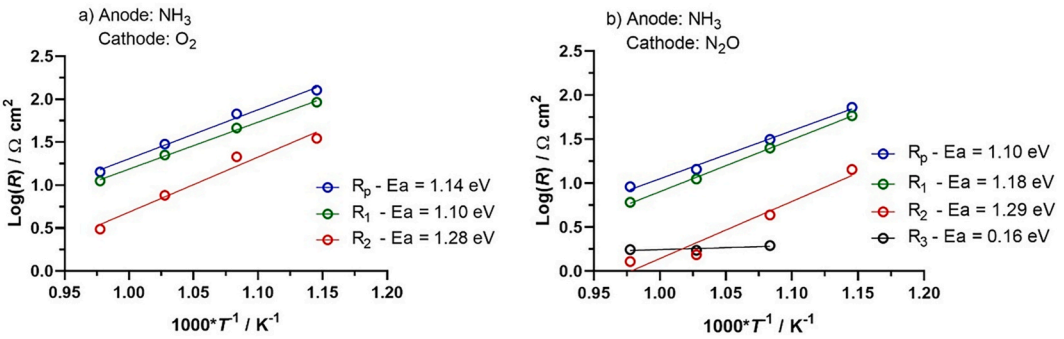


Fig. 6. – The temperature dependence of total (R_p), high-frequency (R_1), intermediate-frequency (R_2), and low-frequency (R_3) polarization resistances at open circuit potential for cell operating under a) NH_3 as fuel and O_2 as oxidant; and b) NH_3 as fuel and N_2O as oxidant, for operation temperature between 600 and 750 °C (E_a depicts the activation energy of each process).

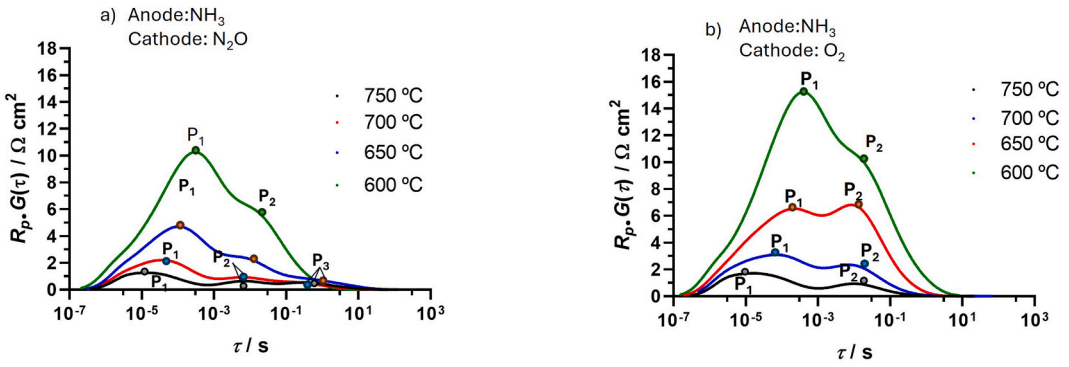


Fig. 7. – Distribution function of relaxation times (DFRT) generated by the *Tikhonov* regularization for cell operating under a) NH_3 as fuel and N_2O as oxidant; and b) NH_3 as fuel and O_2 as oxidant, for operation temperature between 600 and 750 °C.

3.2.2. *Applied polarization conditions*

Fig. 8 a) and b) show the electrode polarization resistances as a function of the applied potential difference (ΔV) at 750 °C when the cell was fed with NH_3/O_2 or with NH_3/N_2O, respectively. Generally, for both oxidants (O_2 and N_2O), the total polarization resistance (R_p) and the polarization resistances R_1, R_2, and R_3, decrease with applied potential difference (ΔV). This was assigned to the increased driving force for the electrochemical reactions [37]. However, R_1 (along with R_p) exhibits an unusual tendency at low applied potentials, where the resistance increases with polarization. This trend causes R_1 to reach a peak at −0.2 V, after which it begins to decrease until −1 V. Such an effect has been observed by several authors for different MIEC cathodes with intrinsically lower ionic conductivities [38], [39], [40]. Therefore, it is likely that this increase in R_1 (and R_p) at low applied potentials results from the ORR process occurring in the SFCMO cathode rather than in (or a combination with) the Ni-YSZ anode.

In particular, this effect may be attributed to variations in the oxygen-vacancy gradient across the electrode under polarization, arising from the different oxygen partial pressures (p_{O_2}). These differences modify the driving force for oxygen transport and, consequently, influence the electrode kinetics [38]. In this regard, the ORR is expected to begin with fast surface gaseous oxygen adsorption

$$O_2(g) \rightarrow O_{2(ads)}(s) \quad (14)$$

and dissociation

$$O_{2(ads)}(s) \rightarrow 2O_{(ads)}(s) \quad (15)$$

on the catalytically active SFCMO, leading to the formation of oxygen adsorbates ($O_{2(ads)}$ and $O_{(ads)}$). This is followed by a first charge transfer step,

$$2O_{(ads)}(s) + 2e^-(s) \rightarrow 2O^-_{(ads)}(s) \quad (16)$$

that proceeds with a final charge transfer and incorporation (surface exchange) into the bulk of the SFCMO phase in the region near the SFCMO/CGO20 interface,

$$2O^-_{(ads)}(s) + 2e^-(s) + V^{\cdot\cdot}_O(s) \rightarrow O^x_O(s) \quad (17)$$

where $V^{\bullet\bullet}_O$ is a doubly charged oxygen vacancy, and O^x_O denotes a regular oxygen ion (O^{2-}) at the normal oxygen position in the lattice. Fig. 9 summarizes this information in a schematic representation of the ORR mechanism.

This surface exchange reaction (Eq. (17)) is directly linked to the ambipolar conductivity of both ionic and electronic terms [41]. This implies that the kinetics of the reactions depend not only on the ability of ions and electrons to move through the bulk of the cathode to the electrolyte, but also on the capacity of the material to adsorb oxygen molecules at its surface, incorporate them as oxygen ions, and transfer ions into the bulk [42]. Therefore, two key parameters are expected to play an important role in these processes: the chemical diffusion (D_{chem}) coefficient, which describes the bulk diffusion of oxygen ions through the cathode lattice, and the surface exchange (K_{ex}) coefficient, which represents the rate at which oxygen molecules from the gas phase are reduced and incorporated into the cathode surface as oxygen ions. Once incorporated, these ions diffuse through the bulk of the solid electrode – the process that is governed by the D_{chem}) [42].

Previous studies have reported a relatively high surface exchange coefficient for SFMO – a parent material of SFCMO, displaying a K_{ex} $\sim 10^{-7}$ cm s^{-1} @ 800 °C and $p_{O_2} = 10^{-2}$ atm [43]. Nevertheless, the

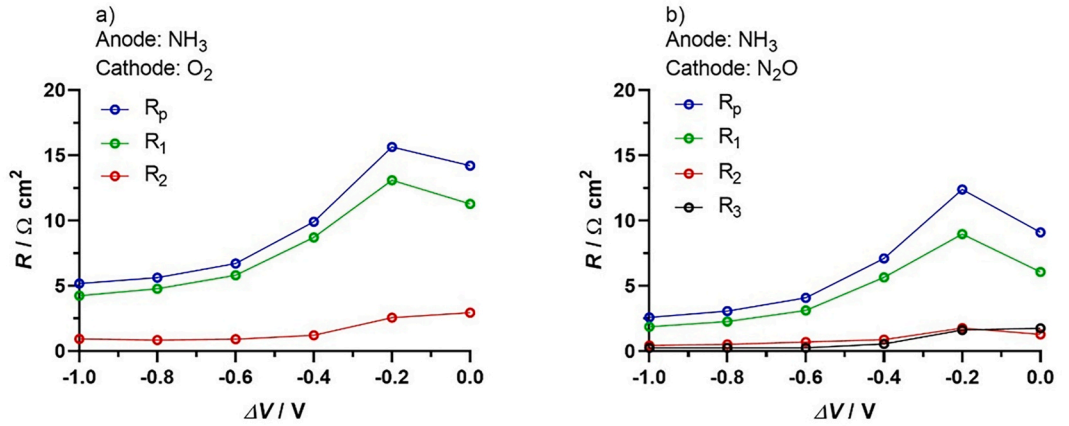


Fig. 8. – Dependence of the applied difference of potential on the SFCMO electrode, at 750 °C, in the total (R_p), high-frequency (R_1), and intermediate-frequency (R_2) polarization resistances at a) NH_3 and O_2 and b) NH_3 and N_2O atmospheres.

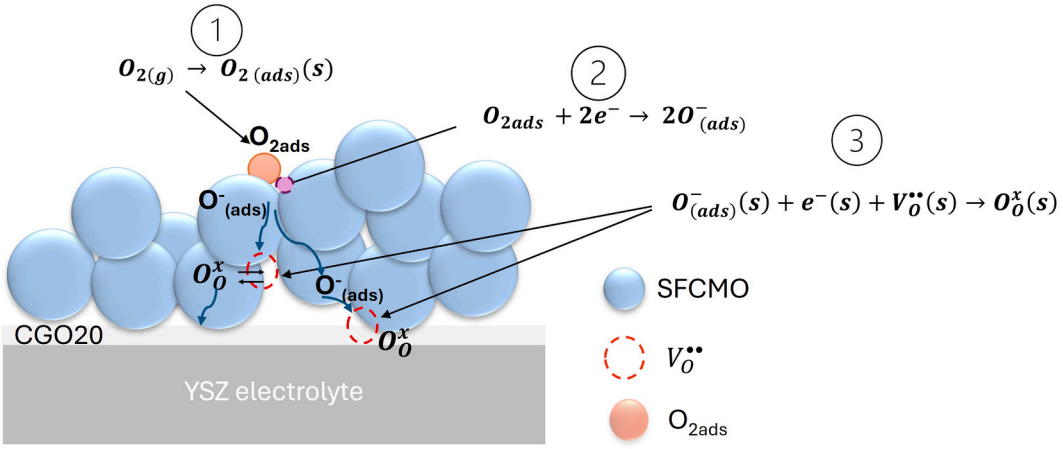


Fig. 9. Overview of the transport mechanism in SFCMO.

corresponding chemical diffusion coefficient is relatively low – D_{chem} $\sim 10^{-8}$ $cm^2\,s^{-1}$ in the same conditions [43]. In comparison, the $Ce_{0.8}Gd_{0.2}O_{2-\delta}$ (CGO) phase – the buffer and adjacent layer – exhibits a much higher chemical diffusion coefficient, in the order of 10^{-4} $cm^2\,s^{-1}$, in the same operating conditions [44], indicating that oxygen ions can move through its lattice several orders of magnitude faster than in SFMO. Consequently, even though SFMO shows favorable surface kinetics, its relatively low bulk diffusion significantly constrains the overall oxygen transport, whereas CGO benefits from both rapid bulk diffusion and reasonably good surface exchange, making it highly effective for oxygen transport applications. Therefore, the oxygen vacancy chemical potential difference (and, consequently, a driving force for oxygen diffusion) cannot be easily maintained across the electrode. Such a scenario justifies the initial increase in R_1 (and, hence R_p) for lower applied potentials. Conversely, under higher applied potentials, this phenomenon is inverted as the vacancies removed from the SFCMO would be rapidly replaced by new vacancies coming from the electrolyte at a rate that ceases to be limited by oxygen surface exchange [38].

Hence, it is proposed that the rate-limiting step in the ORR process is due to the blockage of the active sites at the surface by the occupation of $O^-_{(ads)}$ species during surface exchange (Eq. (17)). The observed behavior can be, thus, considered to occur due to the rapid removal of oxygen vacancies at the electrolyte/electrode interface - Eq. (18), Fig. 10 a) - at a rate higher than that of the surface exchange - Eq. (17), Fig. 10 b).

Therefore, the SFCMO electrocatalyst should possess a high oxygen mobility to attenuate this effect, which can only occur under higher applied potentials. On the other hand, R_2 (mass transport limitations) can be observed to have only a significant decrease in magnitude under low applied potentials. In this case, the vacancy concentration at the electrode/buffer layer interface is expected to increase, according to Eq. (18):

$$V^{\cdot\cdot}_{O(CGO)}(s) + O^x_{O(SFCMO)}(s) \rightarrow V^{\cdot\cdot}_{O(SFCMO)}(s) + O^x_{O(CGO)}(s) \quad (18)$$

However, as ΔV increases further, R_2 becomes essentially independent of the applied polarization, enabling oxygen diffusion through the electrode at a constant rate, while R_1 decreases monotonically. Meanwhile, it is also interesting to note that the magnitude of all polarization resistances is always lower when the cell was fed with NH_3/N_2O (Fig. 8b)), when compared the cell was fed with NH_3/O_2 (Fig. 8a)). The lower polarization resistance observed in N_2O compared to O_2 suggests that oxygen incorporation is kinetically more favorable when N_2O is used as the oxidant. This improvement results from the change in the oxygen concentration gradients, but also to the distinct surface chemistry of N_2O, which decomposes and can form highly reactive oxygen species that may facilitate surface exchange and reduce active-site blockage [45]. Conversely, the lower availability of oxygen in the cathode side (under N_2O atmosphere) provokes the appearance of the low-frequency resistance (R_3), linked to the gas-phase diffusion/conversion limitations.

The lower oxygen reactant concentration prevents the excessive

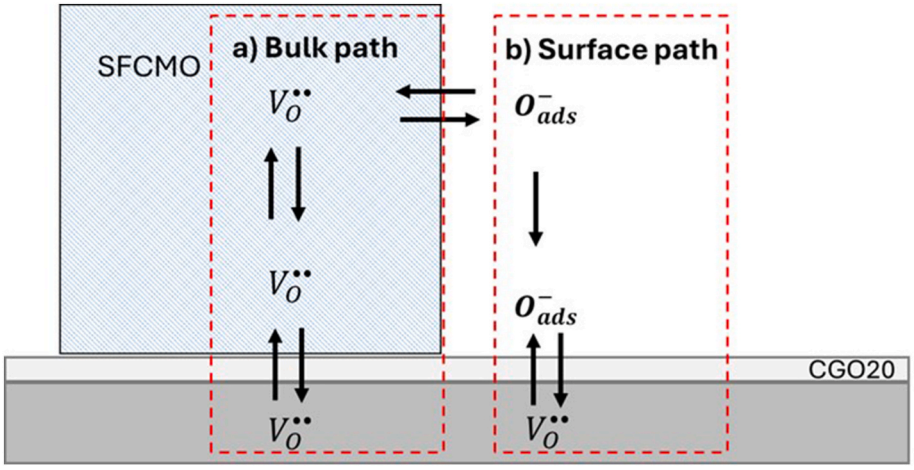


Fig. 10. – a) Oxygen incorporation (surface-exchange) into the SFCMO electrode followed by a direct exchange of oxygen vacancies at the $A_2BB'O_6$/CGO10 interface (oxygen bulk diffusion path); b) Oxygen incorporation (surface-exchange) directly into the CGO20 buffer layer (oxygen surface diffusion path). Adapted from Ref. [39].

accumulation of $O^-_{(ads)}$ species at the electrode's surface. This slows down oxygen vacancy consumption during surface exchange, leading to an increase in the rate of Eq. (17), emphasizing a favorable interdependency that exists between R_3 and R_1 resistances. Conversely, the magnitude of R_3 exhibits a polarization dependence comparable to that of R_2: it decreases with ΔV up to approximately −0.4 V, after which it becomes nearly independent of polarization (Fig. 8b)). The transport of reactants to electrode reaction sites is intrinsically sluggish. Excessive applied potentials intensify concentration polarization, leading to significant depletion of reactants near the electrode surface. This limitation reduces reactant availability for the electrochemical reactions, thereby counteracting the enhanced driving force for the oxygen reduction reaction.

Fig. 11 shows the current–potential (*I-V*) difference characteristics of the cell and corresponding power curves of the SOFC under different oxidizing conditions. When operated with NH_3/N_2O, the cell achieved a peak power density of ~30 mW cm^{-2}, whereas replacing N_2O with O_2 led to a ~30 % decrease in performance (to 21 mW cm^{-2}). This observation aligns well with the impedance results, indicating that the SFCMO cathode exhibits more favorable reaction kinetics under reduced p_{O_2} conditions, owing to lower oxygen vacancy consumption during surface exchange.

The peak power density obtained here (~30 mW cm^{-2} at 750 °C) should be interpreted in light of the specific operating conditions. State-of-the-art H_2-fueled SOFCs reach power densities on the order of 1 W cm^{-2} [46], but these are highly optimized devices operating under conventional oxidizing atmospheres. For NH_3-fueled cells with Ni-YSZ anodes, peak power densities of about 60 - 100 mW cm^{-2} at 750 - 800 °C have been reported [32], [47], which are of the same order of magnitude as the value measured here.

The more relevant comparison concerns the effect of the oxidant. Replacing air by N_2O increased the power output of an H_2-fueled cell by about 50 % [12], and an N_2O-fed $La_{0.6}Sr_{0.4}Co_{0.2}Fe_{0.8}O_{3-\delta}$ – $Gd_{0.1}Ce_{0.9}O_{2-\delta}$ cell delivered ~516 mW cm^{-2} at 650 °C [13]; beyond these two, we identified no other relevant SOFC study using N_2O as oxidant. The ~30 % gain relative to O_2 obtained here is about of the same order, now observed in an NH_3-fed cell with a Co-doped double-perovskite cathode. Those studies, however, did provided limited insight into the individual cathodic processes, as noted in the Introduction. The EIS analysis presented here fills this gap: R_2 decreases about twelve-fold when the cathodic atmosphere is changed from O_2 to N_2O (at OCP and 750 °C), suggesting that N_2O should alleviates the surface-exchange limitation of the SFCMO cathode and thereby leads to a favorable cathodic reaction.

No study addressing N_2O reduction in SOFCs was identified in *Renewable Energy*; the closest related study concerns NH_3-fueled SOFCs operated with air at the cathode [48]. It uses a cobalt-containing $SrCo_{0.5}Fe_{0.45}Ir_{0.05}O_{3-\delta}$ cathode with Pd infiltration to reach 422 mW cm^{-2} at 800 °C on a thin LSGM electrolyte. That route relies on noble metals, and the cathode is reported to have a CTE of 23.2×10^{-6} °C^{-1}, which is substantially higher than the 10.7×10^{-6} °C^{-1} measured for SFCMO. In contrast, the cathode investigated here is a low-Co, noble-metal-free double perovskite, and the performance enhancement is achieved by changing the oxidant rather than modifying the electrode material. Since N_2O reduction replaces the conventional ORR and is coupled to a more complex fuel, a direct benchmark against previous DA-SOFC studies is not straightforward. The modest absolute power density is likely attributable to the manually deposited cathode and the use of diluted NH_3 as the fuel.

The N_2O conversion at 750 °C, calculated from the outlet oxygen partial pressure measured by the zirconia oxygen sensor, across the applied potential range studied, is presented in Fig. 12. N_2O conversion decreases monotonically as the applied potential difference increases, from 42.2 % at −0.2 V to 41.2 % at −1 V. This trend appears to be consistent with competition between N_2O catalytic decomposition and the electrochemical oxygen reduction reaction for shared active surface sites, in agreement with the surface-exchange-limited kinetics discussed above. Notably, the conversion measured at OCP (40.6 %) was lower than that observed in experiments under polarization, indicative of electrochemical activity.

To the best of the authors' knowledge, this is the first reported comparison of N_2O and O_2 as oxidants on the same SFCMO cathode in a DA-SOFC, as previous comparisons were performed in H_2-fueled cells [12], [13]. In addition, the cathode combines a low CTE with the absence of noble metals, and this work provides further insight into the superior performance obtained with N_2O as the oxidant.

Although the overall cell performance is low, the present results support the potential of the proposed cell for coupling pollutant abatement with energy co-generation, and there remains significant scope for improvement through optimization of reactor configuration and cell design.

3.3. Post-mortem analysis

The microstructure of the SFCMO||CGO||YSZ||NiO membrane electrode assembly (MEA) employed in the electrochemical tests was investigated by scanning electron microscopy (SEM) to assess possible morphological aging of the electrodes associated with the cell operation.

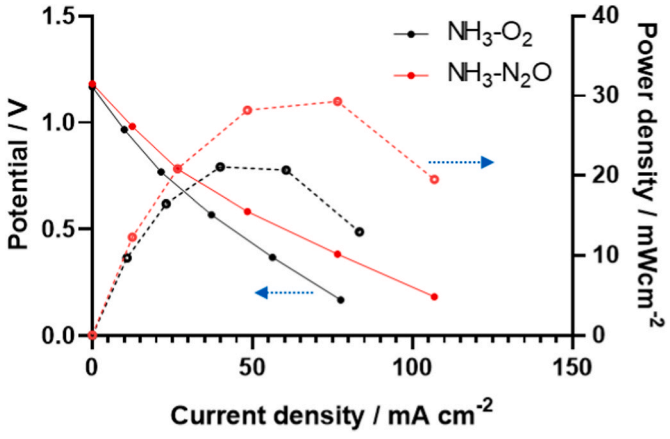


Fig. 11. – Current-potential (*I-V*) characteristics performed at 750 °C, at different working conditions for the cathode and anode: NH_3/O_2 and NH_3/N_2O.

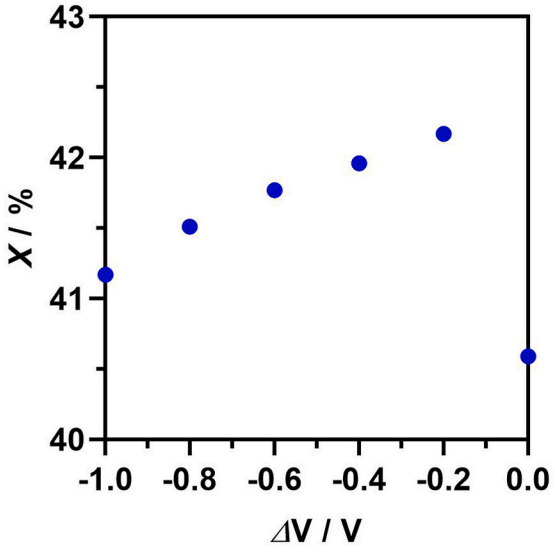


Fig. 12. – Conversion of N_2O (*X*) in the single-cell obtained along the polarization measurements, at 750 °C.

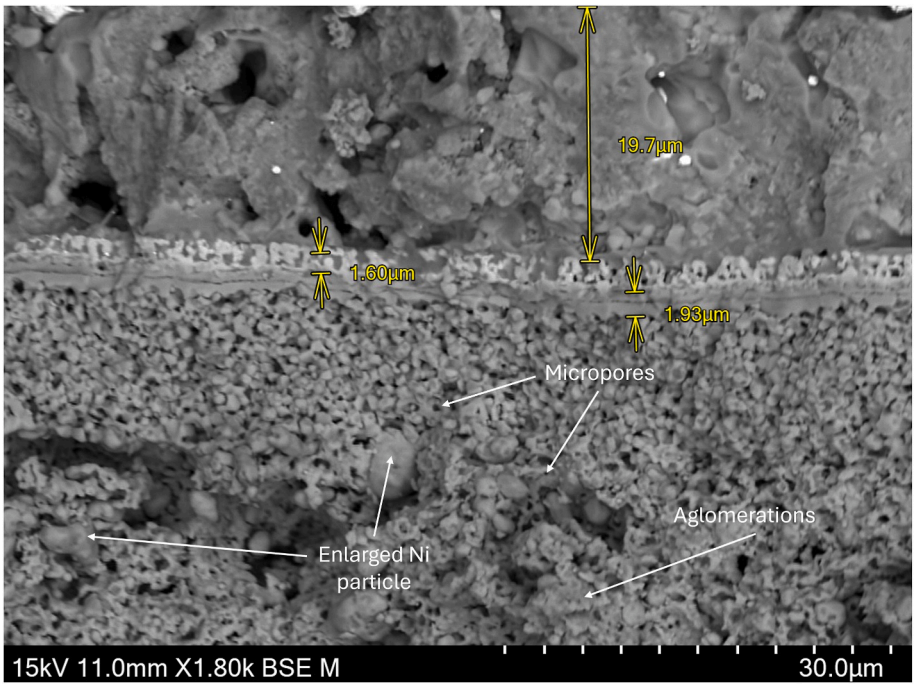


Fig. 13. – Scanning electron microscopy images (SEM) of cross-section microstructure of the MEA: a) cathode - SFCMO, b) buffer layer - CGO, c) electrolyte - YSZ, and d) anode - Ni-YSZ.

Since the same MEA was used for both N_2O and O_2 experiments, the *post-mortem* observations correspond to the final microstructure after exposure to both operating conditions and should not be interpreted as being exclusively associated with either atmosphere. Fig. 13 presents a cross-sectional view of the MEA, highlighting its distinct layers: (a) the cathode composed of the synthesized SFCMO catalyst, with a representative thickness of approximately 19.7 µm, (b) a $Ce_{0.8}Gd_{0.2}O_{2-\delta}$ (CGO) buffer layer, with a representative thickness of approximately 1.60 µm, (c) the YSZ electrolyte with a representative thickness of approximately 1.93 µm, and (d) the Ni-YSZ cermet anode with a nominal thickness of about 396 ± 40 µm, as specified by manufacturer (Elcogen). The SEM image reveals pores in the anode, attributable to the reduction of NiO to metallic Ni, as well as evidence of nickel sintering caused by prolonged exposure to high temperatures [31]; although no long-term durability assessment was performed, the observed Ni coarsening may contribute to a gradual reduction of active triple-phase boundary sites, potentially increasing polarization losses during extended operation. Consequently, dedicated long-term studies are needed to evaluate the evolution of the anode microstructure and its impact on cell performance and durability under realistic operating conditions.

Fig. 14 presents the *post-mortem* energy dispersive spectroscopy (EDS) elemental maps obtained from the MEA cross-section. The elemental distributions confirm that the CGO buffer layer (Ce, Gd) effectively suppressed the migration of strontium from the cathode (Sr, Fe, Co, Mo) towards adjacent layers. As results, the formation of insulating strontium zirconate phases at the cathode-electrolyte interface was effectively mitigated. This is critical because such secondary phases increase interfacial resistance and reduces general SOFC efficiency [49], [50].

4. Conclusions

The $Sr_2Fe_{1.45}Co_{0.05}Mo_{0.5}O_{6-\delta}$ (SFCMO) cathode electrode was successfully prepared via the sol-gel synthesis route followed by calcination in air at 1200 °C, resulting in the formation of a single-phase cubic double-perovskite structure ($Fm\bar{3}m$ space group). Thermogravimetric analysis (TGA) demonstrated good phase stability in air up to 1000 °C, with a small weight loss of 2.2 %, attributed to oxygen loss and associated oxygen vacancies formation, with no evidence of additional mass-loss events indicative of secondary phase decomposition. The developed cobalt-doped cathode (SFCMO) showed a coefficient of thermal expansion (CTE) well matched with common SOFC electrolytes, measuring $10.7 \times 10^{-6}\,°C^{-1}$ *vs* $10.5 \times 10^{-6}\,°C^{-1}$ (for YSZ).

SOFC tests with NH_3 as fuel and O_2 or N_2O as oxidants (600–750 °C) revealed that ORR kinetics are limited by surface active site blockage from adsorbed $O^-_{(ads)}$ species during surface exchange. Lower p_{O_2} in N_2O atmospheres facilitated SFCMO cathode kinetics by reducing oxygen vacancy consumption, yielding ~30 % higher power density than with O_2. Quantitative outlet-gas analysis confirmed an N_2O abatement ~41.7 % across the operation potential range ate 750 °C. These results not only highlight SFCMO as a promising cathode for N_2O reduction for intermediate-temperature ammonia-fueled SOFCs, but also demonstrate that N_2O can serve as electrochemically beneficial oxidant in DA-SOFC operation, rather than merely being regarded as a target pollutant for abatement.

Despite the promising results of this study, further research is needed to improve the practical applicability of SFCMO cathodes. Future efforts should focus on optimizing cathode composition, microstructure, and fabrication procedures to further improve electrochemical activity and to assess long-term durability under realistic NH_3/N_2O operating conditions. In particular, understanding the degradation mechanisms associated with prolonged operation will be essential for evaluating the long-term viability of this material. Such studies will contribute to the development of efficient N_2O-fed ammonia SOFCs capable of simultaneously mitigating greenhouse gas emissions and generating electrical energy, thereby advancing the practical implementation of sustainable energy conversion technologies.

CRediT authorship contribution statement

Celina Fernandes: Writing – original draft, Methodology, Investigation, Formal analysis, Conceptualization. **Laura I.V. Holz:** Writing – review & editing, Methodology, Funding acquisition, Formal analysis. **Francisco J.A. Loureiro:** Writing – review & editing, Funding

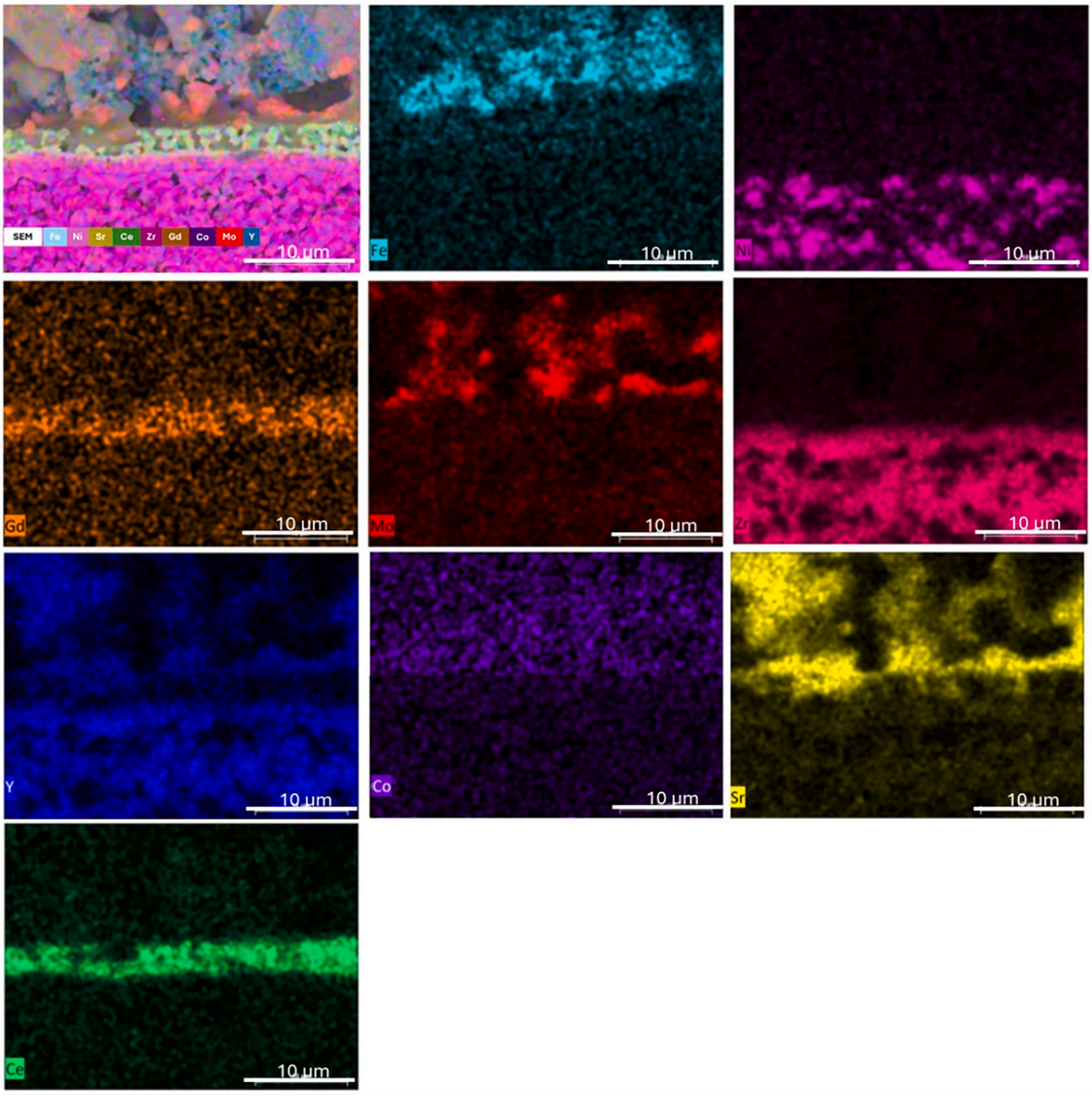


Fig. 14. – EDS mapping images of cross-section microstructure of the MEA.

acquisition, Formal analysis. **Sergey M. Mikhalev:** Methodology, Investigation. **Duncan P. Fagg:** Writing – review & editing, Supervision, Resources, Project administration, Funding acquisition. **Adélio Mendes:** Writing – review & editing, Supervision, Resources, Project administration, Funding acquisition.

Declaration of competing interest

The authors declare that they have no known competing financial interests or personal relationships that could have appeared to influence the work reported in this paper.

Acknowledgments

This work was supported by national funds through FCT/MCTES (PIDDAC): LEPABE, UIDB/00511/2020 (DOI: 10.54499/UIDB/00511/2020) and UIDP/00511/2020 (DOI:10.54499/UIDP/00511/2020) and ALiCE, LA/P/0045/2020 (DOI: 10.54499/LA/P/0045/2020) and under the project/contract UID 00481 - Centre for Mechanical Technology and Automation. This work is a result of project HI_MOV – "Corredor Tecnológico Transfronterizo de Movilidad com Hidrógeno Renovable", with reference 0160_HI_MOV_1_E, cofinanced by European Regional Development Fund (ERDF), through Programa de Cooperação INTERREG VI A Espanha – Portugal (POCTEP) 2021-2027. The authors also acknowledge the following projects: 2022.02498. PTDC (https://doi.org/10.54499/2022.02498.PTDC), 2022.09319. PTDC (https://doi.org/10.54499/2022.09319.PTDC), Celina Fernandes acknowledges FCT for the PhD (2021.07014. BD). Laura Holz and Francisco Loureiro want to acknowledge FCT for their CEEC grants (https://doi.org/10.54499/2023.05868.CEECIND/CP2840/CT0021 and (https://doi.org/10.54499/2020.02797.CEECIND/CP1589/CT0030) and the projects COMPETE2030-FEDER-00744500 16284 2023.17866. ICDT, COMPETE2030-FEDER-00770000 16527 2023.17134. ICDT.

References

[1] L. Alves, et al., A comprehensive review of NOx and N2O mitigation from industrial streams, Renew. Sustain. Energy Rev. 155 (Mar. 2022) 111916, https://doi.org/10.1016/j.rser.2021.111916.

[2] F. Dong, et al., Achieving exceptional activity and durability toward oxygen reduction based on a cobalt-free perovskite for solid oxide fuel cells, J. Energy Chem. 62 (Nov. 2021) 653–659, https://doi.org/10.1016/j.jechem.2021.04.020.

[3] A.I. Osman, et al., Hydrogen production, storage, utilisation and environmental impacts: a review, Environ. Chem. Lett. 20 (1) (Feb. 2022) 153–188, https://doi.org/10.1007/s10311-021-01322-8.

[4] A.G. Margellou, T.C. Vaimakis, P.J. Pomonis, D.E. Petrakis, Catalytic N2O decomposition over La(Sr)FeO3 perovskites, React. Kinet. Mech. Catal. 127 (2) (Aug. 2019) 825–838, https://doi.org/10.1007/s11144-019-01608-7.

[5] M. Bhavisha, et al., Molybdenum incorporated strontium-iron and strontium-cobalt ($SrBMoO_{3-\delta}$; b=fe & co) perovskites: preparation and their application on oxidation of *Iso* -Eugenol into vanillin, Eur. J. Inorg. Chem. 26 (3) (Jan. 2023), https://doi.org/10.1002/ejic.202200590.

[6] W. Jung, H.L. Tuller, A new model describing solid oxide fuel cell cathode kinetics: model thin film $SrTi_{1-x}Fe_xO_{3-\delta}$ mixed conducting Oxides–a case study, Adv. Energy Mater. 1 (6) (Nov. 2011) 1184–1191, https://doi.org/10.1002/aenm.201100164.

[7] Q. Liu, C. Yang, X. Dong, F. Chen, Perovskite Sr2Fe1.5Mo0.5O6−δ as electrode materials for symmetrical solid oxide electrolysis cells, Int. J. Hydrogen Energy 35 (19) (Oct. 2010) 10039–10044, https://doi.org/10.1016/j.ijhydene.2010.08.016.

[8] G. Suchaneck, E. Artiukh, Nonstoichiometric strontium ferromolybdate as an electrode material for solid oxide fuel cells, INORGA 10 (12) (Nov. 2022) 230, https://doi.org/10.3390/inorganics10120230.

[9] X. Pan, Z. Wang, B. He, S. Wang, X. Wu, C. Xia, Effect of Co doping on the electrochemical properties of Sr2Fe1.5Mo0.5O6 electrode for solid oxide fuel cell, Int. J. Hydrogen Energy 38 (10) (Apr. 2013) 4108–4115, https://doi.org/10.1016/j.ijhydene.2013.01.121.

[10] V. Zapata-Ramírez, G.C. Mather, M.T. Azcondo, U. Amador, D. Pérez-Coll, Electrical and electrochemical properties of the Sr(Fe,Co,Mo)O3−δ system as air electrode for reversible solid oxide cells, J. Power Sources 437 (Oct. 2019) 226895, https://doi.org/10.1016/j.jpowsour.2019.226895.

[11] F. Fujishiro, N. Oshima, T. Sakuragi, M. Oishi, Oxygen desorption properties of perovskite-type SrFe1−Co O3−δ: B-site mixing effect on the reduction properties of Fe and Co ions, J. Solid State Chem. 312 (Aug. 2022) 123254, https://doi.org/10.1016/j.jssc.2022.123254.

[12] T. Li, et al., A highly-robust solid oxide fuel cell (SOFC): simultaneous greenhouse gas treatment and clean energy generation, Energy Environ. Sci. 9 (12) (2016) 3682–3686, https://doi.org/10.1039/C6EE02562E.

[13] Y.-T. Rong, et al., Efficient power generation in a solid oxide fuel cell using N2O as the oxidant, Rare Met. 44 (8) (Aug. 2025) 5859–5867, https://doi.org/10.1007/s12598-025-03305-y.

[14] L.I.V. Holz, et al., Strontium iron molybdenum oxide as electrocatalyst for nitrous oxide reduction in solid oxide fuel cells, Int. J. Hydrogen Energy 54 (Feb. 2024) 25–36, https://doi.org/10.1016/j.ijhydene.2023.05.251.

[15] C. Fernandes, L.I.V. Holz, F.J.A. Loureiro, S.M. Mikhalev, D.P. Fagg, A. Mendes, Cobalt doping as a microstructural optimization strategy for Sr2Fe1.5Mo0.5O6-δ cathodes in direct ammonia SOFCs for N2O abatement, Fuel 427 (Jan. 2027) 139812, https://doi.org/10.1016/j.fuel.2026.139812.

[16] Y. Gu, et al., A brief review of high-entropy oxides in solid oxide fuel cell applications, Mater. Sci. Eng., B 327 (May 2026) 119260, https://doi.org/10.1016/j.mseb.2026.119260.

[17] T.H. Wan, M. Saccoccio, C. Chen, F. Ciucci, Influence of the discretization methods on the distribution of relaxation times deconvolution: implementing radial basis functions with DRTtools, Electrochim. Acta 184 (Dec. 2015) 483–499, https://doi.org/10.1016/j.electacta.2015.09.097.

[18] B.A. Boukamp, A. Rolle, Use of a distribution function of relaxation times (DFRT) in impedance analysis of SOFC electrodes, Solid State Ionics 314 (2018) 103–111, https://doi.org/10.1016/j.ssi.2017.11.021.

[19] Atomistic Simulation Group, Data base of Ionic radii [Online]. Available: http://abulafia.mt.ic.ac.uk/shannon/ptable.php. (Accessed 3 June 2025).

[20] D.E. Bugaris, et al., Investigation of the high-temperature redox chemistry of $Sr_2Fe_{1.5}Mo_{0.5}O_{6-\delta}$ via in situ neutron diffraction, J. Mater. Chem. A 2 (11) (2014) 4045–4054, https://doi.org/10.1039/C3TA14913G.

[21] G.Y. Liu, et al., Structural transition and atomic ordering in the non-stoichiometric double perovskite Sr2FexMo2−xO6, J. Alloys Compd. 353 (1–2) (Apr. 2003) 42–47, https://doi.org/10.1016/S0925-8388(02)01316-6.

[22] Q. Liu, et al., Sr2Fe1.5Mo0.5O6−δ as a regenerative anode for solid oxide fuel cells, J. Power Sources 196 (22) (Nov. 2011) 9148–9153, https://doi.org/10.1016/j.jpowsour.2011.06.085.

[23] A.B. Muñoz-García, et al., Unveiling structure–property relationships in $Sr_2Fe_{1.5}Mo_{0.5}O_{6-\delta}$, an electrode material for symmetric solid oxide fuel cells, J. Am. Chem. Soc. 134 (15) (Apr. 2012) 6826–6833, https://doi.org/10.1021/ja300831k.

[24] I. Yasuda, M. Hishinuma, Lattice expansion of acceptor-doped lanthanum chromites under high-temperature reducin'g atmospheres, Electrochemistry 68 (6) (Jun. 2000) 526–530, https://doi.org/10.5796/electrochemistry.68.526.

[25] G.C. Kostogloudis, C. Ftikos, Properties of A-site-deficient La0.6Sr0.4Co0.2Fe0.8O3−δ-based perovskite oxides, Solid State Ionics 126 (1–2) (Nov. 1999) 143–151, https://doi.org/10.1016/S0167-2738(99)00230-1.

[26] A. Ch Lazanas, M.I. Prodromidis, Electrochemical impedance spectroscopy—a tutorial, ACS Meas. Sci. Au 3 (3) (Jun. 2023) 162–193, https://doi.org/10.1021/acsmeasuresciau.2c00070.

[27] E.P. Murray, T. Tsai, S.A. Barnett, Oxygen transfer processes in (La,Sr)MnO3/Y2O3-stabilized ZrO2 cathodes: an impedance spectroscopy study, Solid State Ionics 110 (3–4) (Jul. 1998) 235–243, https://doi.org/10.1016/S0167-2738(98)00142-8.

[28] S. Omar, J.C. Nino, Consistency in the chemical expansion of fluorites: a thermal revision of the doped ceria, Acta Mater. 61 (14) (Aug. 2013) 5406–5413, https://doi.org/10.1016/j.actamat.2013.05.029.

[29] J. Yang, T. Akagi, T. Okanishi, H. Muroyama, T. Matsui, K. Eguchi, Catalytic influence of oxide component in ni-based cermet anodes for ammonia-fueled solid oxide fuel cells, Fuel Cells 15 (2) (Apr. 2015) 390–397, https://doi.org/10.1002/fuce.201400135.

[30] M. Ni, M.K.H. Leung, D.Y.C. Leung, Ammonia-fed solid oxide fuel cells for power generation-A review, Int. J. Energy Res. 33 (11) (Sep. 2009) 943–959, https://doi.org/10.1002/er.1588.

[31] D.S. Dhawale, S. Biswas, G. Kaur, S. Giddey, Challenges and advancement in direct ammonia solid oxide fuel cells: a review, Inorg. Chem. Front. 10 (21) (2023) 6176–6192, https://doi.org/10.1039/D3QI01557B.

[32] O. Elmutasim, D.S. Dhawale, S. Giddey, G. Paul, S. Bhattacharya, Unravelling the reaction mechanism on Ni–YSZ anode supported direct ammonia solid fuel cell: experimental and theoretical studies, Appl. Surf. Sci. 686 (Mar. 2025) 162175, https://doi.org/10.1016/j.apsusc.2024.162175.

[33] A.K. Padinjarethil, F.R. Bianchi, B. Bosio, A. Hagen, Electrochemical characterization and modelling of anode and electrolyte supported solid oxide fuel cells, Front. Energy Res. 9 (Sep) (2021), https://doi.org/10.3389/fenrg.2021.668964.

[34] J.H. Park, H.-N. Im, K.T. Lee, Understanding redox cycling behavior of Ni–YSZ anodes at 500 °C in solid oxide fuel cells by electrochemical impedance analysis, J. Korean Ceram. Soc. 58 (5) (Sep. 2021) 606–613, https://doi.org/10.1007/s43207-021-00136-2.

[35] P.P. deJ, Keeler J. Atkins, Physical Chemistry, twelfth ed., Oxford University Press, 2022.

[36] S. Primdahl, M. Mogensen, Gas diffusion impedance in characterization of solid oxide fuel cell anodes, J. Electrochem. Soc. 146 (8) (Aug. 1999) 2827–2833, https://doi.org/10.1149/1.1392015.

[37] S.W. Boettcher, et al., Potentially confusing: potentials in electrochemistry, ACS Energy Lett. 6 (1) (Jan. 2021) 261–266, https://doi.org/10.1021/acsenergylett.0c02443.

[38] J.R.D. Santos, et al., Understanding the cathodic polarisation behaviour of the misfit [Ca2CoO3−δ]q[CoO2] (C349) as oxygen electrode for IT-SOFC, Electrochim. Acta 285 (Sep. 2018) 214–220, https://doi.org/10.1016/j.electacta.2018.08.018.

[39] A. Svensson, A mathematical model of the porous SOFC cathode, Solid State Ionics 86 (88) (Jul. 1996) 1211–1216, https://doi.org/10.1016/0167-2738(96)00289-5.

[40] D. Pérez-Coll, A. Aguadero, M.J. Escudero, L. Daza, Effect of DC current polarization on the electrochemical behaviour of La2NiO4+δ and La3Ni2O7+δ-based systems, J. Power Sources 192 (1) (Jul. 2009) 2–13, https://doi.org/10.1016/j.jpowsour.2008.10.073.

[41] A. Soultati, K. Aidinis, A. Chroneos, M. Vasilopoulou, D. Davazoglou, Ambipolar surface conduction in oxygen sub-stoichiometric molybdenum oxide films, Sci. Rep. 13 (1) (Nov. 2023) 21166, https://doi.org/10.1038/s41598-023-48060-1.

[42] C. Endler-Schuck, J. Joos, C. Niedrig, A. Weber, E. Ivers-Tiffée, The chemical oxygen surface exchange and bulk diffusion coefficient determined by impedance spectroscopy of porous La0.58Sr0.4Co0.2Fe0.8O3−δ (LSCF) cathodes, Solid State Ionics 269 (Jan. 2015) 67–79, https://doi.org/10.1016/j.ssi.2014.11.018.

[43] D.A. Osinkin, A.V. Khodimchuk, N.M. Porotnikova, N.M. Bogdanovich, A. V. Fetisov, M.V. Ananyev, Rate-determining steps of oxygen surface exchange kinetics on Sr2Fe1.5Mo0.5O6−δ, Energies 13 (1) (Jan. 2020) 250, https://doi.org/10.3390/en13010250.

[44] K. Yashiro, Mass transport properties of Ce0.9Gd0.1O2−δ at the surface and in the bulk, Solid State Ionics 152–153 (Dec. 2002) 469–476, https://doi.org/10.1016/S0167-2738(02)00375-2.

[45] N. Swadchaipong, et al., Study of nitrous oxide utilization for syngas production *via* partial oxidation of methane using Ni-doped perovskite catalysts, RSC Adv. 15 (5) (2025) 3080–3088, https://doi.org/10.1039/D4RA06805J.

[46] J. Zhang, S. Ricote, P.V. Hendriksen, Y. Chen, Advanced materials for thin-film solid oxide fuel cells: recent progress and challenges in boosting the device performance at low temperatures, Adv. Funct. Mater. 32 (22) (May 2022), https://doi.org/10.1002/adfm.202111205.

[47] G.G.M. Fournier, I.W. Cumming, K. Hellgardt, High performance direct ammonia solid oxide fuel cell, J. Power Sources 162 (1) (Nov. 2006) 198–206, https://doi.org/10.1016/j.jpowsour.2006.06.047.

[48] A. Alveal, et al., Study of the performance of SrCo0.50Fe0.45Ir0.05O3-δ cathodes for intermediate temperature solid oxide fuel cells (IT-SOFC) fueled by hydrogen and ammonia, Renew. Energy 276 (Nov. 2026) 126399, https://doi.org/10.1016/j.renene.2026.126399.

[49] S. Lee, K. Lee, J. Lee, J. Lee, T. Kim, J. Bae, Evaluation of electrolyte materials of Gd- and Ce-Doped scandia-stabilized zirconia and Yb- and Bi-Doped gadolinium-doped ceria for highly durable solid oxide fuel cells, International Journal of Precision Engineering and Manufacturing-Green Technology 11 (4) (Jul. 2024) 1217–1228, https://doi.org/10.1007/s40684-023-00577-6.

[50] A. Hessler-Wyser, Z. Wuillemin, J.A. Schuler, A. Faes, J. Van herle, TEM investigation on zirconate formation and chromium poisoning in LSM/YSZ cathode, J. Mater. Sci. 46 (13) (Jul. 2011) 4532–4539, https://doi.org/10.1007/s10853-011-5347-5.